Rare Metal Materials and Engineering
Volume 54, Issue 11, November 2025
Available online at www.rmme.ac.cn

Science Press

Cite this article as: Zhang Changqing, Ma Dongdong, Gu Huaizhuang, et al. Microstructural Evolution and Strengthening Mechanisms of Shoulderless Micro-friction Stir Welded Joints of 1060-H24 Pure Aluminum[J]. Rare Metal Materials and Engineering, 2025, 54(11): 2757-2767. DOI: https://doi.org/10.12442/j.issn.1002-185X.20240586.

ARTICLE

Microstructural Evolution and Strengthening Mechanisms of Shoulderless Micro-friction Stir Welded Joints of 1060-H24 Pure Aluminum

Zhang Changqing[1,2], Ma Dongdong[2], Gu Huaizhuang[2], Wang Dong[2], Liu Enrong[2], Zhang Pengsheng[3]

[1] State Key Laboratory of Advanced Processing and Recycling of Nonferrous Metals, Lanzhou University of Technology, Lanzhou 730050, China; [2] School of Materials Science and Engineering, Lanzhou University of Technology, Lanzhou 730050, China; [3] Northwest Institute for Nonferrous Metal Research, Xi'an 710016, China

Abstract: The differences between shouldered and shoulderless tools in the micro-friction stir welding of 0.8 mm thin plates were evaluated. Employing a suite of advanced characterization methods, including white light interferometry, electron backscatter diffraction (EBSD), and scanning electron microscopy, the formation of weld surface, joint microstructure distribution, and fracture characteristics were studied. The enhancement mechanism of mechanical properties was explained through the Hall-Petch relationship and Taylor's hardening law. Results indicate that the main reason for the increased yield strength observed in shoulderless tool joints is the combined mechanism of dislocation strengthening and fine-grain strengthening. Specifically, the utilization of shouldered tools results in a smooth weld surface, with an average grain size of 11.24 μm and a high-angle grain boundary content of 16.80% in the nugget zone. The primary texture components are the {011}<100> Goss and {112}<111> copper textures, yielding a maximum texture strength of 3.70. Simultaneously, the fracture dimples exhibit a reduction in size and an increase in depth. Whereas the welds produced with shoulderless tools display slight burrs on the surface. The experimental results demonstrate that the average grain size in the nugget zone of these joints is significantly reduced to 0.59 μm, while the high-angle grain boundary content reaches 34.34%. This process is accompanied by the formation of {111}<110> Shear textures and {001}<110> rotated cubic textures as the main components, resulting in a significant increase in maximum texture strength to 6.65.

Key words: micro-friction stir welding; stirring tool; EBSD; mechanical properties

1 Introduction

Friction stir welding (FSW), an advanced solid-state joining technique, was pioneered by the Welding Institute (TWI) in the United Kingdom in 1991[1]. This method overcomes common flaws in traditional fusion welding, including solidification cracks, microsegregation, and porosity. Considering the burgeoning demand for ultra-thin accuracy welds, a comprehensive understanding of the correlation between FSW conditions and resultant microstructures is paramount. Through accurate control of heat input variability, weld performance can be optimally tailored[2].

In 2004, Nishihora et al[3] pioneered a method based on the FSW process for joining thin-walled structural materials with thicknesses below 1 mm, which was named as micro-friction stir welding (μFSW). However, the annealing softening effect induced by residual heat after μFSW process reduces dislocation density and promotes grain growth in the heat-affected zone (HAZ) of ultra-thin plate welds. This phenomenon thus creates a weak point in the joint[4]. Process parameters, including welding and rotation speeds, along with stirring tool morphology, are commonly modulated to reduce these drawbacks and achieve superior joint microstructure and mechanical properties. Ni et al[5] employed a pinless tool on

Received date: November 06, 2024
Foundation item: National Nature Science Foundation of China (52261013)
Corresponding author: Zhang Pengsheng, Ph. D., Professor, Northwest Institute for Nonferrous Metal Research, Xi'an 710016, P. R. China, E-mail: zhangpengsheng2015@163.com

AA7075-T6 aluminum alloy with the thickness of 0.5 mm, and observed that as rotation speed increases from 2000 r/min to 8000 r/min, the high-temperature exposure duration of the post-welding joint increases correspondingly. Therefore, the average grain size in the weld nugget zone (NZ) expands from 1.72 μm to 2.08 μm, while the recrystallization content and high-angle grain boundary content in this zone decrease by 4.091% and 4.410%, respectively. Xu et al[6] evaluated microstructural evolution across varying heat inputs during the post-welding air cooling stage utilizing heat treatment methods, and indicated that the initially large grains in the base material (BM) experience significant shear deformation at higher temperatures, yielding optimized grains characterized by high dislocation density. During the following air cooling, static recovery occurs, prompting dislocation annihilation, grain growth, and changes in texture type. Kalinenko et al[7] utilized electron backscatter diffractometer (EBSD) to analyze the microstructural evolution of 6061 aluminum alloy joint with a thickness of 3 mm. Results indicated that continuous recrystallization governs grain structure evolution in the stir zone or NZ. All rotational speeds cause plastic deformation. Dislocations in sub-grain regions are absorbed at the low-angle grain boundaries (LAGBs) during deformation caused by FSW. As this process continues, the misorientation of the initial LAGBs increases. As more dislocations are absorbed, eventually a large amount of misorientation reaches the 15° threshold, amount of which is used to define high-angle grain boundaries (HAGBs) by EBSD. Dutta et al[8] conducted pinless friction stir welding on AA6061-T6 plates with a thickness of 0.5 mm, developing a three-dimensional (3D) numerical analysis model through ABAQUS to evaluate the effect of equivalent plastic strain on microstructural evolution utilizing EBSD. The study demonstrated that incorporating the pin enhances plastic strain. Compared to the joint welded without the pin tool, the average grain size in the weld NZ is reduced by 2.4 times, while the HAGB fraction is increased by 2.8%. Wang et al[9] evaluated the effect of grain size on mechanical properties utilizing EBSD and the Hall-Petch relationship. An optimization of average grain size of BM from 17.5 μm to 2.35 μm yields a 1.01 and 0.7 GPa increase in yield strength and tensile strength, respectively. This reduction in grain size also results in a 46.3% decrease in fracture strain and an increase in microhardness to 255.22 HV. They indicated that grain optimization and dislocation strengthening contribute 109.5 and 654.1 MPa to the yield strength, respectively. These correlations between welding temperature, the resultant grain structure in the stir zone, and the overall mechanical properties suggest that the welding thermal cycle is the primary factor governing microstructure evolution in friction stir welds. The analysis of heat generation models for conventional stirring tools by Schmidt[10] and Gadakh[11] et al indicated that the stirring pin generates 24% of the total heat input. Similarly, the research by Zhang et al[12] demonstrated that the measured peak heat of the welding joint with shoulderless tool is only 24.9% of that with traditional tools. Therefore, utilizing only the stirring pin during processing can significantly reduce heat input to the joint. Moreover, compared to traditional FSW, the flash produced during shoulder insertion is eliminated, thereby avoiding weld thinning and enhancing mechanical properties. However, it is important to acknowledge that the potential benefits offered by the pin tool are most fully realized when welding thin plates. As the thickness increases, the likelihood of an unwelded defect at the bottom of the weld increases due to insufficient heat input.

This study evaluates the potential of shoulderless μFSW to enhance the mechanical properties of weld joints. By reducing heat input during the welding process, the objective is to achieve a finer grain structure, thereby increasing strain rate, improving the mechanical properties of the weld NZ, and reducing softening in HAZ. A comparative analysis of weld surfaces produced by shoulderless and conventional tools was conducted utilizing a white light interferometer. Secondly, EBSD and scanning electron microscope (SEM) were employed to characterize microstructural differences between the joints produced by the two methods, including grain size, grain boundary distribution, and texture type. Finally, the study provided a potential explanation for the superior microhardness and yield strength observed in the shoulderless tool joints based on established principles, such as the Hall-Petch relationship and Taylor's hardening law.

2 Experiment

AA1060, commercially designated as a pure aluminum alloy, comprises greater than or equal to 99.6% Al. The designation T24 signifies the applied heat treatment process. In this designation, 2 denotes natural aging of the aluminum alloy, while 4 indicates that the alloy has been subjected to a controlled cooling and artificial aging process to enhance its hardness and strength. The chemical composition of the AA1060-H24 pure aluminum is detailed in Table 1. This experiment involved the butt welding of two plates, each measuring 140 mm×25 mm×0.8 mm. Two WC-Co carbide tools, each with a shoulder diameter of 6 mm, were utilized for the welding process. The tool pin exhibited a truncated cone shape, with upper and lower base diameters of 2 and 1 mm, respectively. The stirring pins in the shouldered and shoulderless tools were 0.6 and 0.8 mm in length, respectively. During the μFSW process, parameters were maintained as follows: tool rotation speed of 12 000 r/min, welding velocity of 240 mm/min, and inclination angles of 2.5° and 0° for shoulder and shoulderless tools, respectively. The welding procedure comprised four stages: plunging, dwelling, welding, and exiting. In the plunging phase, the shoulder tool was positioned at an inclination angle of 2.5°, and the depth of the shoulder plane plunge into the weldment was 0.06 mm; whereas when utilizing the shoulderless tool,

Table 1 Chemical composition of BM (wt%)

Si	Fe	Cu	Mg	Mn	Zn	Ti	V	Al
0.15	0.20	0.05	0.03	0.03	0.05	0.03	0.03	Bal.

the inclination angle was set at 0° , only the stirring pin engaged with the weldment, achieving a penetration depth of 0.8 mm, while the shoulder plane remained clear of the weldment. Fig. 1a offers a schematic diagram of the welding process, while Fig. 1b details the dimensions of the two stirring tools.

The restricted thickness of the plate precluded direct embedding of the thermocouple at the designated weldment location. Therefore, a 1.5 mm blind hole, aligned with the weld NZ of the joint, was machined into the surface of the backing plate utilizing computer numerical control machining. A K-type thermocouple was then inserted into this blind hole, ensuring that the thermocouple contacts were positioned as near as possible to the workpiece surface. These contacts were secured utilizing high-temperature adhesive. The sensor and conditioning circuit converted the physical welding temperature signal into a voltage signal of 0–5 V. The data

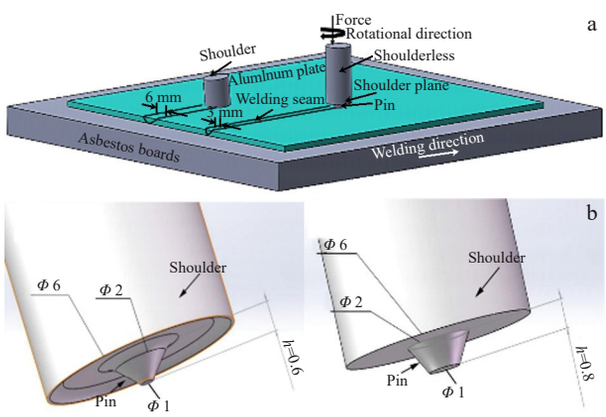

Fig.1 Schematic diagram of μFSW process (a) and dimensions of the two stirring tools (b)

was recorded through the NI USB-6218 data acquisition card and LabView software produced by National Instruments (NI) in the United States. A sampling rate of 10 000 Hz was employed for the NI USB-6218, and a corresponding formula facilitated the conversion of the acquired data into temperature values.

Weld surface topography was captured with a digital camera. Simultaneously, a white light interferometer was utilized to generate a local 3D profile centered on the weld surface. Fracture morphology observations were conducted utilizing a FEG-450 thermal field emission SEM. For samples in the EBSD analysis, standard metallographic methods were employed during the pre-polishing stage. Then, these samples were subjected to electropolishing in a solution of 25% nitric acid in methanol. The electropolishing process utilized a voltage of 20 V and a duration of 60 s. Microstructural analysis was then conducted utilizing a JMS-F100 SEM, and the data analysis was performed utilizing Channel 5 software. Joint mechanical properties were evaluated employing a WA-1000B universal tensile testing machine and a VH-1000 microhardness tester (loading force: 500 g, duration: 10 s). Due to the susceptibility of the ultra-thin 1060 aluminum plate to deformation, a pneumatic clamp, rather than a conventional clamp, was used to secure the tensile specimens to reduce potential joint damage. A tensile speed of 0.5 mm/min was maintained throughout testing.

3 Results and Discussion

3.1 Weld surface topography and welding temperature

Fig. 2a and 2d illustrate the weld surface topographies, while Fig. 2b and 2e present the localized 3D profiles along the weld centerline. Regarding weld surface with shoulder tools, a minor degree of flash is evident at the joint edges.

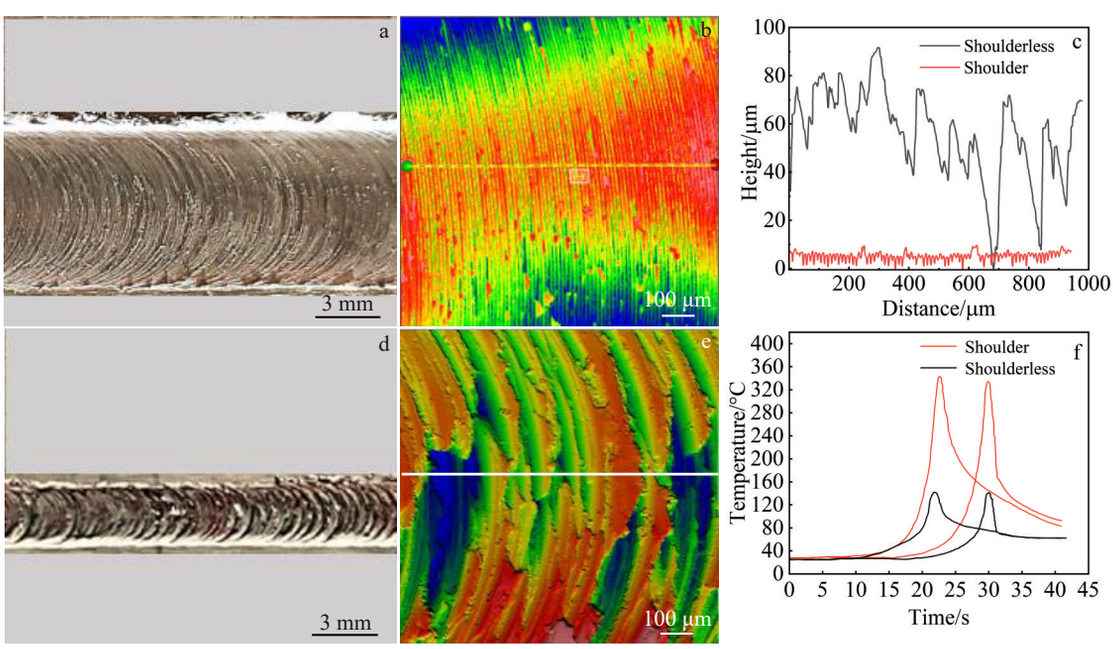

Fig.2 Topographies (a, d) and 3D contours (b, e) of weld surface with shoulder tool (a–b) and shoulderless tool (d–e); (c) profile curves of joint parallel to weld direction; (f) thermal cycle curves of joint

Moreover, the thermoplastic material fills the cavity located behind the stirring pin, which is facilitated by the shoulder plane. This process yields a smooth weld surface characterized by a consistent arc pattern. On the contrary, joints welded utilizing shoulderless tools exhibit no flash. Simultaneously, the presence of surface burrs is noted, leading to a significant expansion of the distance between arc marks. Fig. 2c displays the stacking height of the thermoplastic material, along with the arc spacing parallel to the weld direction. Owing to the dissimilar outer diameters of the two tools, both the advance per revolution and the surface velocity at the maximum diameter are different. The distance between the peaks and valleys of the joint with shoulder tools is measured approximately 7 μm, while the arc spacing is estimated roughly 20 μm. However, in the joints welded utilizing shoulderless tools, the peak-to-valley distance is increased to approximately 80 μm, accompanied by an arc spacing of roughly 58 μm. Fig. 2f displays the measured thermal cycle curves of the joint. During the stable welding stage, the peak temperature in the weld NZ reaches approximately 346 ° C for conventional tools, whereas it registers only 131 °C for shoulderless tools. This discrepancy causes a bulging of the welding surface, thereby increasing the spacing between the arc lines. Specifically, the characteristics of the thin plate prevent the direct embedding of the thermocouple in the weld NZ. Simultaneously, the high-temperature adhesive acts as a barrier between the thermocouple and BM, finally resulting in a measured temperature lower than the actual welding temperature. The friction between the shoulder plane and the BM enhances metal plasticization. The inclined and concave shoulder plane facilitates the effective smoothing of this plasticized metal in the weld zone through backfilling and extrusion. Simultaneously, the shoulders, acting as constraints, compel the material to adopt a radial outward flow pattern (in a spiral pattern); whereas, the absence of shoulders directs the material towards the back of the pin, generating a hump that distends the welding surface and broadens the inter-arc spacing. This phenomenon originates from the design of the shoulderless tool, which cannot impart backfilling and extrusion effects on the thermoplastic material due to the lack of a shoulder plane. Accordingly, the thermoplastic material accumulates on the front surface of stirring pin. Upon reaching a critical height, this accumulated material detaches from the stirring pin, and then forms burrs through a natural cooling and crystallization process.

3.2 Grain size and orientation

It can be observed from the microstructure distribution of the weld NZ of the two joints (Fig. 3) that the BM and the weld NZs produced by the shoulder tool and the shoulderless tool exhibit unique microstructural characteristics. Fig. 3a presents the inverse pole figure (IPF) of the BM, while Fig.3b and Fig. 3c illustrate IPFs of the weld NZs produced by the shoulder and shoulderless tools, respectively. Grain size statistics, obtained by fitting the major axis of the ellipse, are presented in Fig. 3d. Specifically, both welding tools result in joints with a fine recrystallized structure compared to the BM. However, the average grain size of the joints welded utilizing shoulderless tools is significantly smaller, measuring only 0.59 μm; whereas, the presence of the shoulder plane during welding leads to a significant increase in average grain size, reaching 11.24 μm. This difference can be attributed to the high-stress generated during the welding process with shoulderless tools and the prolonged high-temperature duration induced by the shoulder tools, which promotes the growth of recrystallized grains in the weld NZ. IPFs,

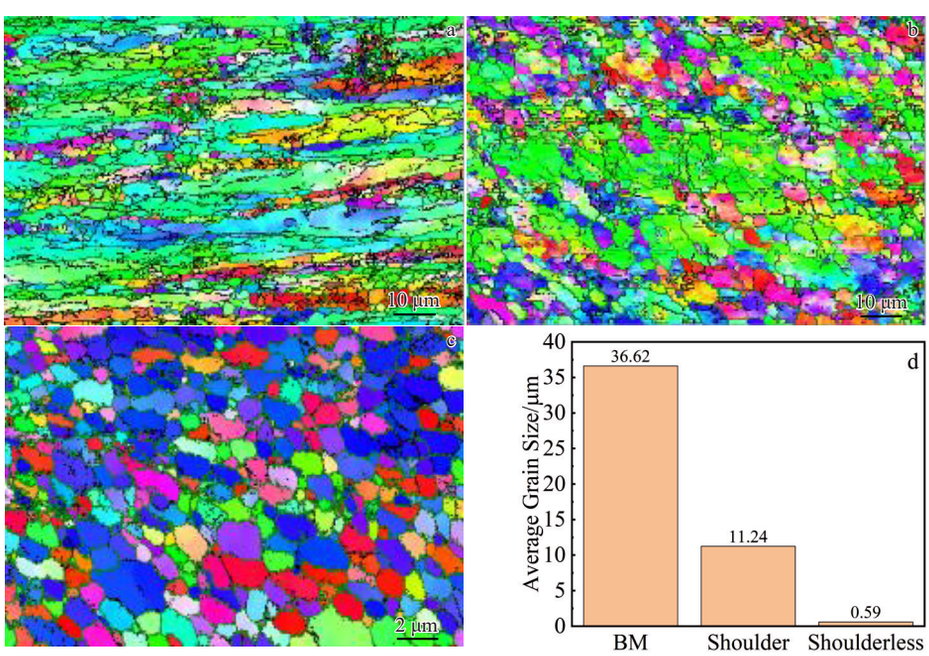

Fig.3 IPFs (a – c) and average grain size statistics (d) of BM (a) and the weld NZs produced by the shoulder tool (b) and shoulderless tool (c)

employing different colors to represent unique crystal orientations, indicate that the grains in the BM exhibit an elongated state, primarily aligning along the <101> direction. This preferred orientation arises from the slip behavior of face-centered cubic (fcc) metals, which typically occurs along the close-packed direction on the close-packed plane, specifically the {111} <101> slip system. This slip system offers the least resistance to slip due to the extremely close distance between atoms. Therefore, when subjected to deformation forces, metals tend to slip along this system, resulting in the observed preferred orientation. The thermal-mechanical coupling in the μFSW process significantly affects the grain orientation of the BM. Joints welded by shoulderless tools primarily exhibit the <111> orientation, whereas those welded with shoulder tools display a mainly <101> orientation and a mixed orientation between <101> and <111>.

3.3 Recrystallization and grain boundary distribution

Fig. 4 presents a metallographic image depicting the ND×TD cross-section, in which TMAZ means thermo-mechanically affected zone, AS and RS denote the advancing side and retreating side of the welded joint, respectively. In the joint with shoulderless tool, the length of weld NZ is 0.8 mm, which is similar to the surface diameter of the stirring pin. The HAZ demonstrates inward shrinkage, reflecting as a configuration wider at the top and progressively narrowing towards the base. In contrast, the joint with the shoulder tool exhibits a weld NZ measuring 3.2 mm in length, a value that falls between the diameters of the stirring pin and the shoulder plane. This observation suggests that the shoulder plane contributes to a two-fold effect. On the one hand, it generates more heat, thereby promoting material plasticization. On the other hand, it expands the material flow range, resulting in an enlarged weld NZ. Compared to the weld joints with shoulderless tools, the integration of the shoulder plane in the BM intensifies weld thinning. Such mechanical thinning, as evidenced by research of Meng et al[13], can significantly reduce the load-bearing capacity of weld.

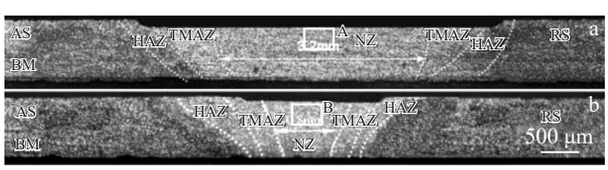

Fig.4 Metallographic images of ND×TD cross-section of welds with shoulder tool (a) and shoulderless tool (b)

To investigate the evolution mechanisms of the microstructure in welded joints fabricated with different stirring tools, EBSD analysis was conducted. The scanning regions are designated as zones A and B in Fig.4. Fig.5 offers a visual representation of the recrystallized grain and grain boundary distribution in the weld NZ. Fig.5 uses black curves to represent HAGBs, denoting grain boundaries with an orientation difference exceeding 15° ; while green curves depict LAGBs, which are characterized by an orientation difference in the range of 2° – 15° . Quantitative analysis, as depicted in Fig.5d, indicates that HAGBs of the BM constitute 72.5%. The constituents of the BM comprise recrystallized (8.93%), sub-structured (48.82%), and deformed (42.24%) grains.

The research of Huang et al[14] indicated that the high rotational velocity of the stirring tool induces both plastic deformation and strain in the joint. These factors contribute to the initiation of recrystallization, i. e., the morphology of elongated and rolled grains transforms into optimized and equiaxed grains. In the continuous dynamic recrystallization process, variations in orientation contribute to the formation

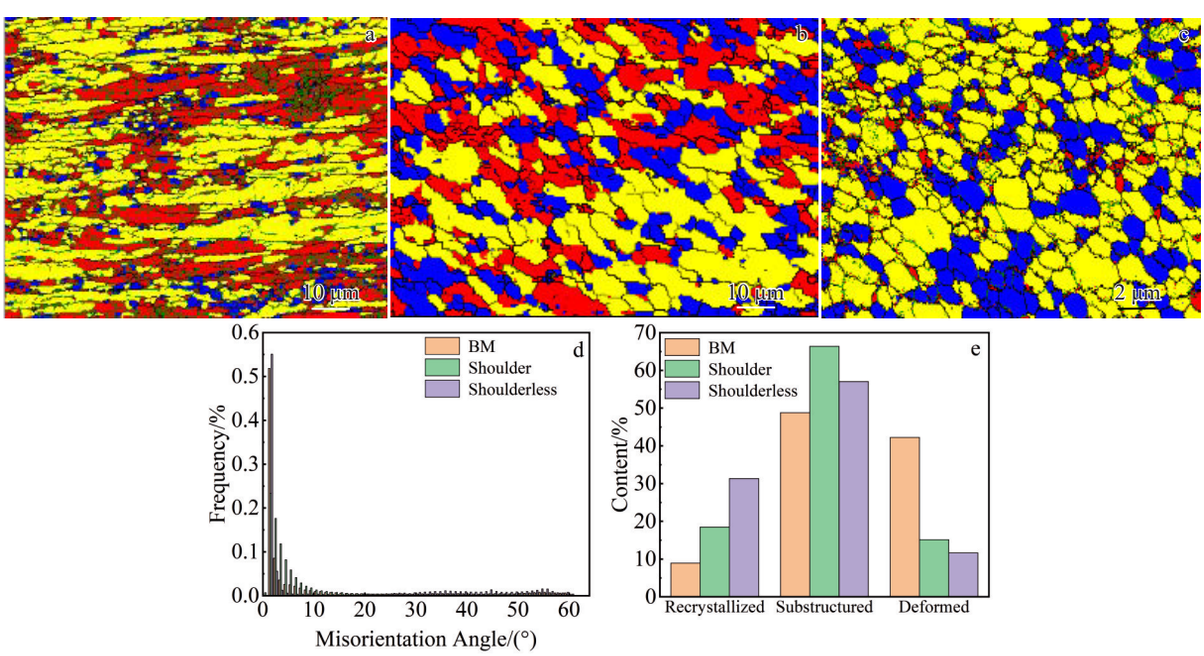

Fig.5 Distribution maps of recrystallized grain and grain boundary in the weld NZ of BM (a) and welds with shoulder tool (b) and shoulderless tool (c); quantitative analysis of misorientation angle distribution (d) and contents of different grains (e)

of LAGBs. The persistent plastic deformation further facilitates the evolution of LAGBs into HAGBs through a mechanism involving dislocation absorption. During mechanical tensile testing of the joints, a tendency for grain rotation towards the <101> crystallographic direction is observed, corresponding to the atomic close-packing direction. However, this reorientation is impeded by grain boundaries. A higher density of non-<101>-oriented grains exacerbates this repeated grain boundary obstruction, which macroscopically translates into enhanced yield strength and reduced plastic deformation. Statistical analysis of the recrystallization grain and grain boundaries is shown in Fig. 5d. It indicates that the joints with shoulderless tool exhibit a recrystallization content of 31.33%, surpassing the 18.47% observed in joints with shoulder tool; whereas the sub-structured grain content is lower in joint with shoulderless tool (57.02%) compared to that with shoulder tool (66.38%). This aligns with the findings of Xu et al[17], who suggested that the presence of shoulder plane elevates heat input to the joint, prolonging its exposure time to high temperatures and promoting the high-temperature static growth of recrystallized grains in the weld NZ. Static recovery primarily involves dislocation movement towards lower energy configurations. Dislocations initially situated on the slip plane form subgrain boundaries through slipping and climbing, effectively reducing dislocation density. With increasing welding heat input, LAGBs absorb dislocations and experience increased misorientation, facilitating their transformation into HAGBs[18]. Therefore, joint with shoulderless tool exhibits a higher HAGBs content (34.34%) compared to that with shoulder tool (16.80%).

3.4 Texture type and content

Through rotation and alignment procedures, the shear direction and shear plane of various weld joint areas were mapped onto the standard ideal texture to facilitate analysis[15]. As depicted in Fig. 6a, the BM exhibits a high degree of similarity with the ideal standard texture, primarily composed of Shear, Brass, and S textures, with a peak texture strength reaching 8.67. Fig. 6b and 6c illustrate the <100>, <101>, and <111> pole figures for the weld NZs of the joints with shoulder tool and shoulderless tool, respectively. Specifically, the pole figure of the joint with shoulder tool displays a uniform color distribution with a high degree of dispersion, indicating a broader distribution of crystal orientation and a weaker texture strength in this region; whereas the color distribution in the weld NZ of the joints with shoulderless tool is largely concentrated in a specific zone, signifying an enhancement in texture strength. Table 2 presents the predominant texture types and their corresponding content for the BM and both tool joints, which are determined through analysis and statistical evaluation utilizing Channel 5 software.

As evidenced by Table 2, the welding process conducted with different stirring tools yields significant changes in the texture type and content. Joints welded utilizing a shoulder tool primarily exhibited {011}<100> Goss, {112}<111> Copper, and {124}<211> S textures, with a peak texture strength of 3.70. In contrast, joints welded with a shoulderless tool developed textures including {111}<110> Shear, {001}<110> rotated cubic, and {112}<111> Copper textures, achieving a

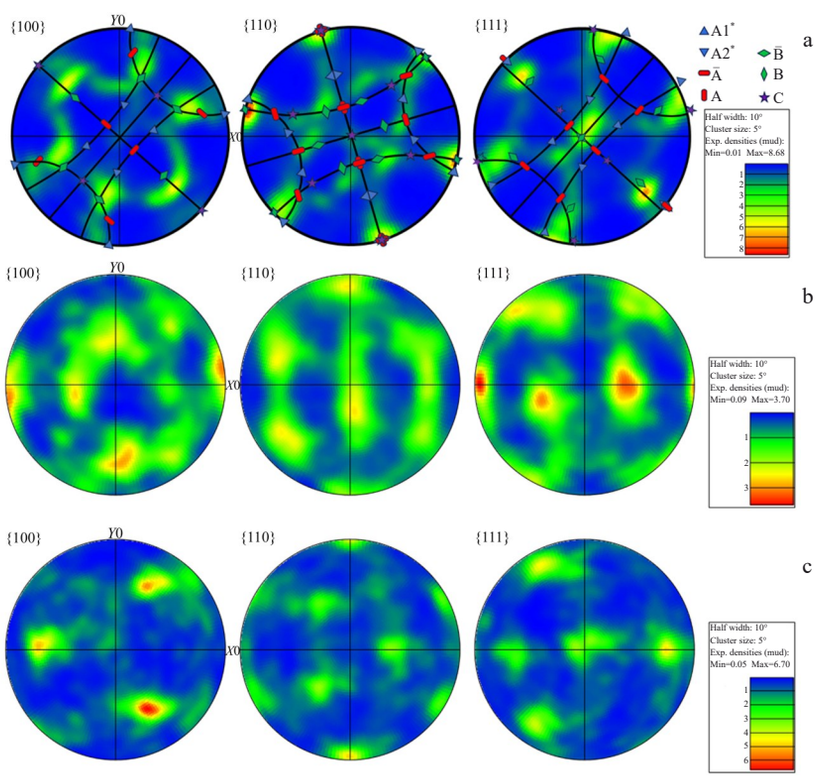

Fig.6 Pole figures of weld NZs of BM (a) and joints with shoulder tool (b) and shoulderless tool (c)

Table 2 Predominant texture content/%

Texture	BM	Shoulder	Shoulderless
{001}<110>	3.71	0.84	11.20
{111}<110>	13.90	6.47	31.30
{001}<100>	1.16	2.99	0.63
{124}<211>	3.53	19.70	4.27
{011}<211>	10.60	11.60	6.98
{011}<100>	14.30	15.30	5.29
{112}<111>	1.82	21.60	16.70

maximum texture strength of 6.65. It is worth noting that the {111}<110> Shear texture constitutes a significant percentage (up to 31.3%) in welded joints with shoulderless tool, comparing with welded joints with shoulder tool. This discrepancy aligns with findings of Liu et al[19], who suggested that the Shear texture in FSW joints correlates with the flow stress generated during the welding process. Lower joint temperatures correspond to increased flow stress, thereby increasing the difficulty of material deformation. As only the stirring pin contributes to heat generation, the overall heat input in the joint with shoulderless tool is reduced, further inhibiting material deformation. Pure aluminum, characterized by a fcc structure, exhibits a close-packed {111} plane and a close-packed <110> direction. These directions, with the lowest surface energy, result in a {111}<110> Shear texture with minimal resistance to movement. This characteristic could explain the increase or concentration of this specific texture in shoulderless tool welded joints.

3.5 Microhardness, yield strength, and fracture morphology

Fig. 7a illustrates the microhardness profiles of joints welded with different tools, which present completely different distribution trends. The joint with shoulder tool exhibits a unique W-shaped microhardness profile. Specifically, near the HAZ-TMAZ, the microhardness value reduces to 35 HV, indicating the softening characteristic of joint welding. However, in the NZ, the microhardness value peaks at 39 HV, which is attributed to grain optimization arising from comprehensive recrystallization; whereas the welded joint with shoulderless tool exhibits a peak-type microhardness distribution. Here, the microhardness value adjacent to the HAZ-TMAZ zone remains at approximately 43 HV, effectively reducing joint softening. In the NZ, the microhardness value increases to 63 HV, marking a significant increase of 43% compared to the BM microhardness (44 HV).

Fig. 7b presents the force-displacement curves of the joints with different tools. The experimental data indicate that the joint with the shoulderless tool attains a yield strength of approximately 338.5 MPa, representing a significant enhancement of 114 MPa (33.7%) compared to BM. However, with the incorporation of the shoulder plane, the yield strength declines to 233.4 MPa, which is slightly higher than that of BM. Fracture morphology analysis was conducted by an FEG-450 thermal field SEM, and the results are displayed in Fig. 8. Both joints exhibit a layered fracture

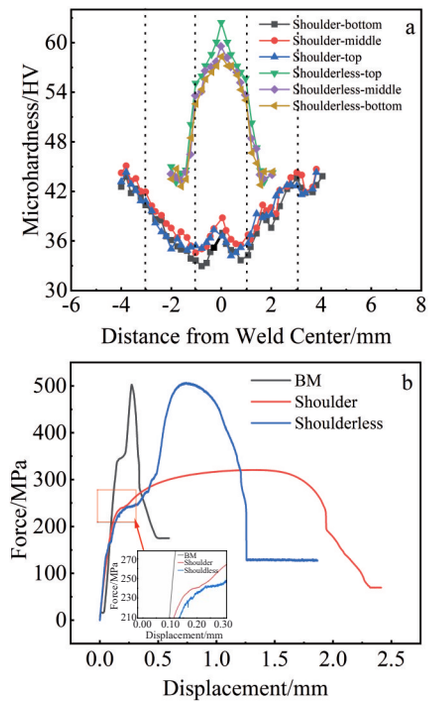

Fig.7 Microhardness distribution contours (a) and force-displacement curves (b) of BM and joints welded with different tools

morphology characterized by a mixed fracture configuration comprising dimples and cleavage surfaces. Analysis of the fracture surface indicates that the joint with shoulder tool presents relatively smaller and deeper dimples, indicating enhanced joint plasticity. As depicted in Fig.5, the presence of the shoulder plane results in the joint experiencing higher welding temperatures, leading to the transformation of some HAGBs into LAGBs. While this transformation reduces the texture strength of joint, it simultaneously enhances the plasticity[16]. In the absence of the shoulder plane, a more significant delamination phenomenon is observed on the fracture surface characterized by a reduction in number of dimples and shallower depth. This difference can be attributed to the lower heat generation associated with shoulderless tools, which accordingly restricts the plasticization range of metal and produces uneven flow between the upper and lower microstructures.

Through transmission electron microscope (TEM) analysis, Liu et al[20] established a relationship between dislocations and microhardness. Their research demonstrated that the microhardness of the weld NZ originates from dislocation strengthening, with a higher dislocation density yielding a more significant strengthening effect. This phenomenon originates from the increased dislocation density acting as an impediment to crystal slip, thus enhancing the material's resistance to deformation. In pure aluminum, when the dislocation content of the joint surpasses that of the BM, the result is reflected in an increase in microhardness; whereas a softening of the joint is observed. Geometrically necessary dislocations (GNDs) describe dislocations necessitated within a

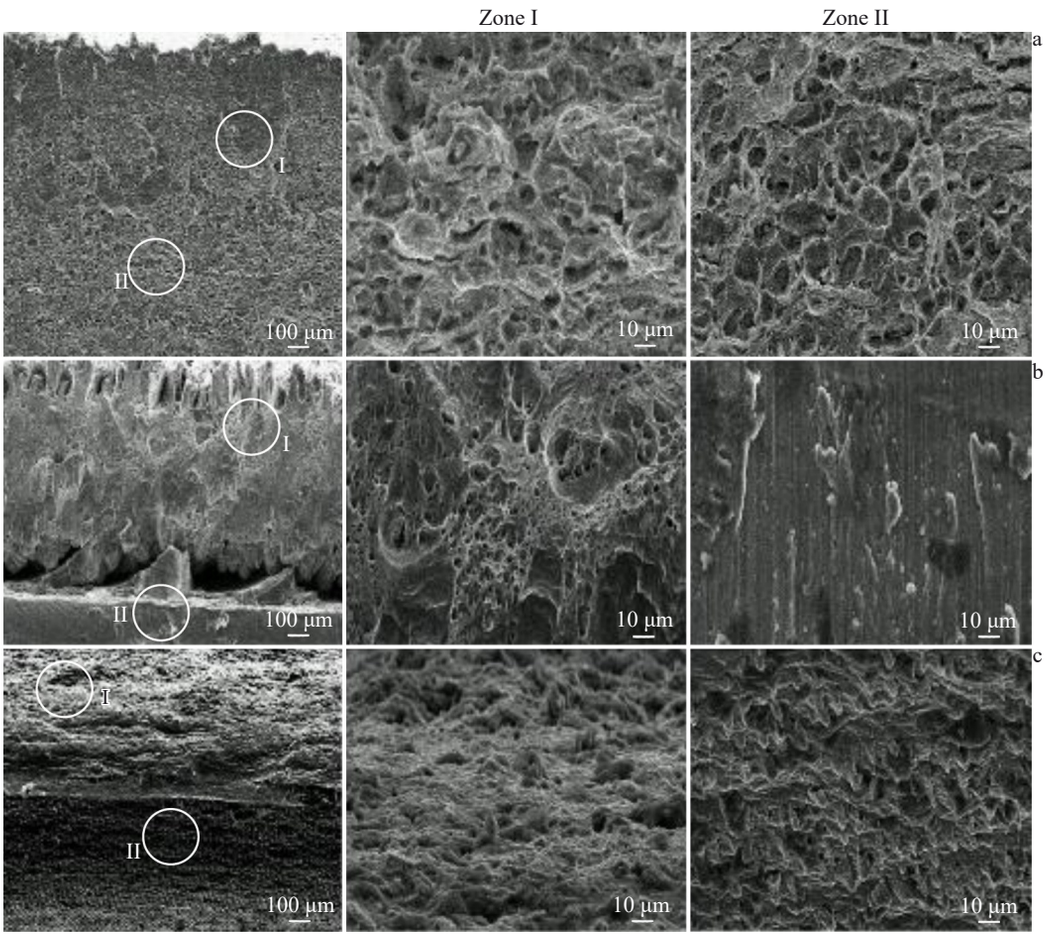

Fig.8 Fracture morphologies of BM (a) and joints with shoulder tool (b) and shoulderless tool (c)

material during plastic deformation by geometrical constraints or heterogeneous deformation, which constitutes the total dislocation density of the material collectively with statistically stored dislocations (SSDs). Considering that SSDs are primarily located in the grain, the main contribution to dislocation enhancement arises from GNDs. In a study conducted by Zaiser et al[21], the kernel average misorientation (KAM) was employed to determine the local GND content in the joint, as detailed in Eq. (1):

$$\rho_{GND} = 2\Phi/\mu \boldsymbol{b} \quad (1)$$

where μ represents the scan step size employed during the EBSD measurement; $\boldsymbol{b}$ denotes the Burgers vector; Φ signifies the average KAM value for each joint. Considering the fcc lattice structure of the pure aluminum, $\boldsymbol{b}$ is determined by multiplying the lattice parameter (0.405 nm) by $\sqrt{2}/2$[22]. Fig. 9a – 9c illustrate the KAM distributions for the BM and both joint configurations. Utilizing Channel 5 software, a statistical analysis of KAM distribution was conducted, focusing on the weld NZ of each joint. The corresponding statistical outcomes are presented in Fig.8b.

Analysis of the KAM distribution and statistical data indicates a KAM value of 2.51 for the joint with shoulder tool, indicating significant stress and strain concentration. A previous study by Akbari et al[23] can support this finding employing Deform 3DTM software to explore the effect of the shoulder plane on strain during the welding process. Their analyses demonstrated that frictional heat generated by the shoulder plane induces localized softening in the joint, thereby promoting strain accumulation; whereas in the case of shoulderless tools, heat generation is primarily localized to the stirring pin. This reduced heat input helps maintain a KAM value of joint with shoulderless tools similar to that of BM, aligning with the experimental observations of Zaiser et al[21]. The calculation results of the joint ρ_{GND} are demonstrated in Fig. 9e. The BM exhibits a ρ_{GND} value of 31.01×10^{-15} m^{-2}, while the joints with shoulderless tool and shoulder tool yield ρ_{GND} values of 285.71×10^{-15} and 6.99×10^{-15} m^{-2}, respectively. To evaluate the anti-deformation characteristics of the different joint configurations, a VH-1000 microhardness tester (under a loading force of 0.2 N and load duration of 10 s) was used. Simultaneously, a white-light interferometer was employed to obtain 3D profiles of each indentation point. The results are depicted in Fig. 10. As ρ_{GND} increases, the material exhibits enhanced resistance to deformation under a constant load. The high heat input associated with the shoulder tool joints promotes softening in the joint region, resulting in a maximum deformation height of approximately 12.2 μm. In contrast, the reduced heat input characteristic of the joint with shoulderless tool reduces softening defects and facilitates an

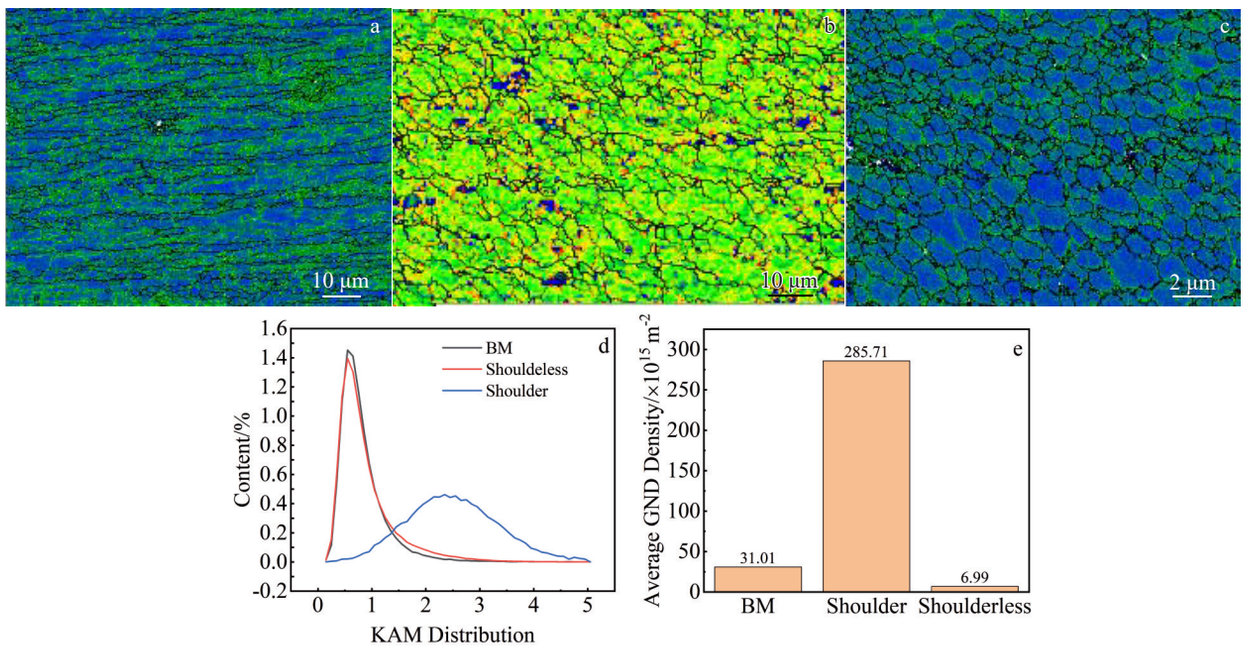

Fig.9 KAM maps of BM (a) and joints with shoulder tool (b) and shoulderless tool (c); quantitative analysis of KAM distribution (d) and average GND density (e)

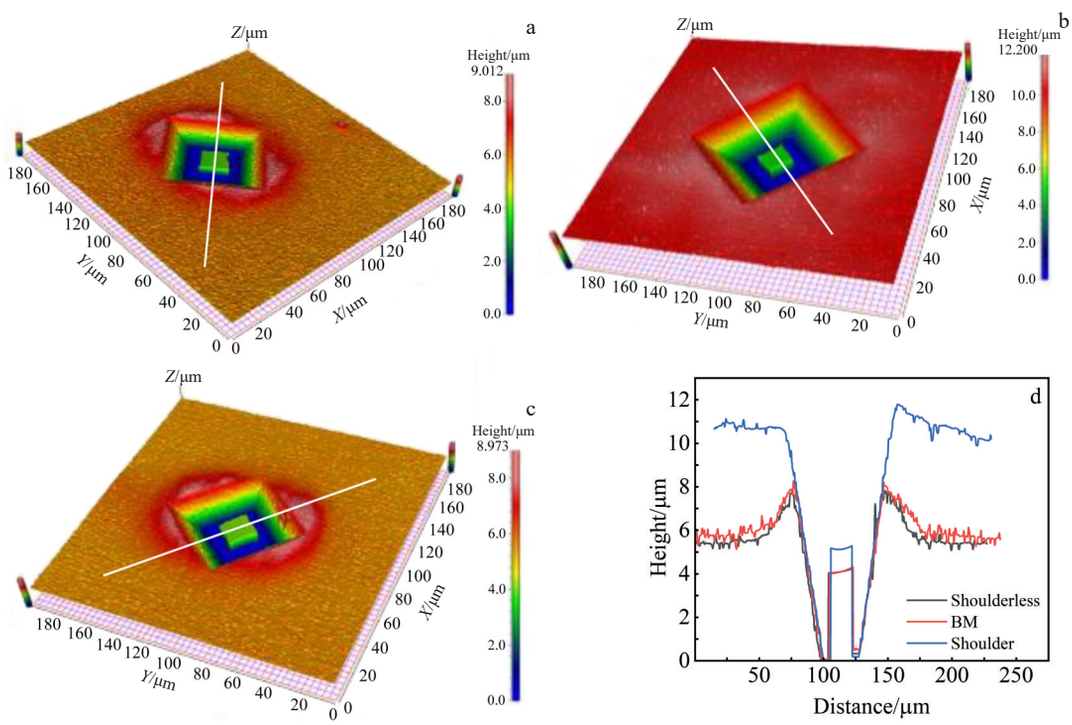

Fig.10 3D contours (a–c) and corresponding statistical outcome (d) of microhardness test points: (a) BM; (b) joint with shoulder tool (c) joint with shoulderless tool

increase in dislocation density. Therefore, compared to the BM, an improvement in deformation resistance is observed with a maximum deformation height of only 8.975 μm.

The experimental procedures employed 1060 pure aluminum, which is a material devoid of precipitation or solid solution strengthening mechanisms. Therefore, the observed enhancement in yield strength is primarily attributed to the combined effects of fine-grain strengthening and dislocation strengthening. This mechanism can be explained as follows:

$$\sigma_y = \sigma_g + \sigma_{dis} \quad (2)$$

where σ_y represents the yield strength of the joint, σ_g represents the contribution of the fine-grain strengthening mechanism to the yield strength of the joint, and σ_{dis} is the

contribution of the dislocation strengthening mechanism to the yield strength of the joint. According to the Hall-Petch equation[24], the contribution of the fine-grain strengthening mechanism could be calculated:

$$\sigma_g = k\left(d^{-0.5} - d_0^{-0.5}\right) \quad (3)$$

where d_0 and d are the initial grain size and post-weld grain size, respectively. The Hall-Petch relationship with a constant k of 1060 can effectively characterize the behavior of the 1060 pure aluminum[25–26]. As illustrated in Fig. 3, the initial grain size of the plate is 36.62 μm, while the post-weld joints with shoulderless tool and shoulder tool exhibit grain sizes of 0.59 and 11.24 μm, which indicates that the contribution of the fine-grain strengthening mechanism is 39.67 and 4.64 MPa to the joint yield strength, respectively. In addition, the contribution of dislocation strengthening to the joint yield strength can be explained using Taylor's hardening law[27]:

$$\sigma_{dis} = M\alpha G\boldsymbol{b}\rho^{0.5} \quad (4)$$

where M is the Taylor factor, α represents an empirical constant, G denotes the shear modulus, $\boldsymbol{b}$ symbolizes the Burgers vector, and ρ signifies the dislocation density. Specifically, the shear modulus of pure aluminum is approximately 25 GPa[28]. For pure aluminum sheets, M can be calculated as follows:

$$M = (1 + 0.5\ln A)/(1 - A^2) \quad (5)$$

where A represents the strain in the equivalent area. In plates, strain refers to the deformation per unit length and is typically derived from a force-displacement curve, as depicted in Fig. 7b. The yield strength calculation results are shown in Fig. 11.

As summarized in Fig. 11, dislocation strengthening contributes 3.24 and 49.96 MPa to the yield strength of joints fabricated with shoulder and shoulderless tools, respectively. The calculated yield strengths for the joints with shoulderless tool and shoulder tool are 313.53 and 231.78 MPa, respectively. These values are slightly lower than the experimentally measured strengths of 338.5 and 233.4 MPa, with a maximum discrepancy of 7.4%. Similar calculations performed by Wang et al[9] also yielded an estimated yield strength that was approximately 0.24 GPa lower than the actual measured value. This underestimation was attributed to lattice defects, which was verified through TEM analysis.

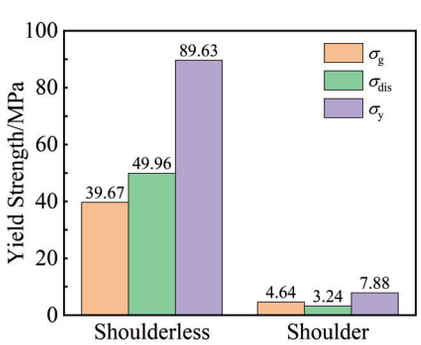

Fig.11 Yield strength calculation results

4 Conclusions

1) The low heat input delivered to joints with shoulderless tool during the welding process produces an average grain size of only 0.59 μm, effectively preserving the optimized grains. In contrast, due to the significant heat input and extended high-temperature exposure, joints with shoulder tool exhibit static recovery of the optimized equiaxed grains in the NZ after welding that leads to a significantly larger average grain size of 11.24 μm.

2) The microhardness profile of joints with shoulder tool displays a W-shaped characteristic, indicating a significant softening defect. Moreover, the percentages of HAGBs and equiaxed crystals in the NZ of these joints is 16.80% and 18.47%, respectively. With a maximum texture strength of 3.70, the principal texture components include the {011}<100> Goss texture, {112}<111> Copper texture, and {124}<211> S texture. Whereas, joints with shoulderless tool exhibit a peak-type microhardness profile, effectively minimizing softening defects. This improvement is accompanied by an increase in the percentage of HAGBs and equiaxed crystals in the NZ to 34.34% and 31.33%, respectively. These joints, characterized by a maximum texture strength of 6.65, develop the {111}<110> Shear texture, {001}<110> rotated cubic texture, and {112}<111> Copper texture.

3) The yield strength of joints with shoulderless tool demonstrates an increase of 114.6 MPa compared to that of the BM. Calculations suggest that fine-grain strengthening and dislocation strengthening mechanisms contribute 39.67 and 49.96 MPa to this increase, respectively. As the heat input decreases, the failure mode of the joint becomes more significant, with a corresponding decrease in number and depth of dimples, signifying reduced plasticity. In contrast, the incorporation of the shoulder plane results in a marginal increase in yield strength of joints with shoulder tool relative to the BM. This increase is attributed to the fine-grain strengthening mechanism (4.64 MPa) and the dislocation strengthening mechanism (3.24 MPa). Moreover, the presence of the shoulder plane reduces failure and increases both the number and depth of dimples, indicating enhanced plasticity.

References

1 Thomas W M, Nicholas E D, Needham J C. *UK Patent*, 9125978[P]. 1991

2 Cavaliere P, Cabibbo M, Panella F. *Materials & Design*[J], 2009, 30(9): 3622

3 Mishra R S, Ma Z Y. *Materials Science and Engineering R*[J], 2005, 50(1–2): 1

4 Wang Y F, Jian A, Kun Y. *Acta Metallurgica Sinica*[J], 2018, 31(8): 878

5 Ni Y, Fu L, Shen Z *et al*. *Journal of Manufacturing Processes*[J], 2019, 48: 145

6 Xu N, Chen L, Feng R N *et al*. *Journal of Materials Research and Technology*[J], 2020, 9(3): 3746

7 Kalinenko A, Vysotskiy I, Malopheyev S *et al*. *Materials Characterization*[J], 2021, 178: 111202

8 Dutta A, Pal S K, Panda K S. *Materials Today Communications*[J], 2023, 38: 17600

9 Wang J Y, Zou J P. *Materials Characterization*[J], 2022, 193: 112254

10 Schmidt H J B, Hattel J, Wert J. *Modeling and Simulation in Materials Science and Engineering*[J], 2003, 12: 143

11 Gadakh V S, Adepu K. *Journal of Materials Research and Technology*[J], 2013, 2(4): 370

12 Zhang C Q, Wang W J, Jin X *et al*. *Metals*[J], 2019, 9: 507

13 Meng X C, Huang Y X, Cao J *et al*. *Progress in Materials Science*[J], 2021, 115: 100706

14 Huang K, Logé R E. *Materials & Design*[J], 2016, 111: 548

15 Fonda R W, Knipling K E. *Acta Materialia*[J], 2010, 58(19): 6452

16 Peng Y, Zhang Q, Wen L Y *et al*. *Metals*[J], 2022, 12(2): 201

17 Xu N, Chen L, Liu K L. *Journal of Mechanical Engineering*[J], 2022, 58(24): 3746

18 Swathi B, Sujay Aadithya B, Balachandar K. *World Journal of Engineering*[J], 2020,17(6): 795

19 Liu X C, Sun Y F, Nagira T *et al*. *Materialia*[J], 2019, 6: 100302

20 Liu X Q, Liu H J, Yu Y. *Acta Metallurgica Sinica*[J], 2020, 33(1): 115

21 Zaiser M, Aifantis E C. *Scripta Materialia*[J], 2003, 48(2): 133

22 Gazizov M, Belyakov A, Holmestad R *et al*. *Acta Materialia*[J], 2023, 243: 118534

23 Akbari M, Aliha M R M, Berto F. *Forces in Mechanics*[J], 2023, 10: 100166

24 Hansen N. *Scripta Materialia*[J], 2004, 51(8): 801

25 Satyanarayana M, Kumar A, Kethavath K. *Journal of Materials: Design and Applications*[J], 2004, 235(9): 2151

26 Novitskaya E, Karandikar K, Cummings K *et al*. *Journal of Materials Research and Technology*[J], 2021, 11: 823

27 Lu S L, Kan Q H, Zhang B *et al*. *Materials Today Communications*[J], 2022, 33: 104580

28 Restasari A, Ardianingsih R, Abdillah L H. *Iranian Polymer Journal*[J], 2023, 32(10): 1347

1060-H24纯铝无肩微搅拌摩擦焊接头的显微组织演化与强化机制

张昌青[1,2]，马东东[2]，谷怀壮[2]，王　栋[2]，刘恩荣[2]，张鹏省[3]

(1. 兰州理工大学 省部共建有色金属先进加工与再利用国家重点实验室，甘肃 兰州 730050)

(2. 兰州理工大学 材料科学与工程学院，甘肃 兰州 730050)

(3. 西北有色金属研究院，陕西 西安 710016)

摘　要：评估了0.8 mm薄板微搅拌摩擦焊中带肩和无肩工具的差异。采用白光干涉法、电子背散射衍射和扫描电子显微镜等一系列表征方法，研究了焊缝表面形成、接头微观组织分布和断裂特征。通过Hall-Petch关系和Taylor硬化定律解释了力学性能的增强机制。结果表明，无肩工具接头屈服强度提高的主要原因是位错强化和细晶强化的综合机制。具体而言，使用轴肩工具可获得光滑的焊缝表面，平均晶粒尺寸为11.24 μm，焊核区大角度晶界含量为16.80%，观察到的主要织构组分为{011}<100> Goss织构和{112}<111> Copper织构，最大织构强度为3.70，同时断口韧窝尺寸减小、深度增加。而无肩工具焊缝表面出现轻微毛刺，试验结果表明，该类接头焊核区平均晶粒尺寸显著减小至0.59 μm，大角度晶界含量达到34.34%，并伴随以{111}<110>剪切织构和{001}<110>旋转立方织构为主要组分的形成，导致最大织构强度显著提高至6.65。

关键词：微型搅拌摩擦焊；搅拌工具；电子背散射衍射；力学性能

作者简介：张昌青，男，1973年生，博士，研究员，兰州理工大学省部共建有色金属先进加工与再利用国家重点实验室，甘肃 兰州 730050，E-mail：zhangcq@lut.edu.cn